OPEN ACCESS
IOP Publishing
Journal of Physics D: Applied Physics
J. Phys. D: Appl. Phys. 54 (2021) 165107 (7pp)
https://doi.org/10.1088/1361-6463/abddf8

Combined SEM-CL and STEM investigation of green InGaN quantum wells

B Ding*, **J Jarman, M J Kappers and R A Oliver***

Department of Materials Science and Metallurgy, University of Cambridge, 27 Charles Babbage Road, Cambridge CB3 0FS, United Kingdom

E-mail: bd371@cam.ac.uk and rao28@cam.ac.uk

Received 14 September 2020, revised 19 December 2020
Accepted for publication 20 January 2021
Published 5 February 2021

Abstract

The microstructure of green-emitting InGaN/GaN quantum well (QW) samples grown at different temperatures was studied using cross-section scanning transmission electron microscopy (STEM) and plan-view cathodoluminescence (CL). The sample with the lowest InGaN growth temperature exhibits microscale variations in the CL intensity across the sample surface. Using STEM analysis of such areas, the observed darker patches do not correspond to any observable extended defect. Instead, they are related to changes in the extent of gross-well width fluctuations in the QWs, with more brightly emitting regions exhibiting a high density of such fluctuations, whilst dimmer regions were seen to have InGaN QWs with a more uniform thickness.

Keywords: gallium nitride, green LEDs, quantum well, TEM, cathodoluminescence, AFM

(Some figures may appear in colour only in the online journal)

1. Introduction

Conventional green LEDs combine blue/ultra-violet LEDs and phosphor wavelength converters, and emit green light via fluorescence processes. There are many advantages of this approach such as good stability and competitive pricing. However, the importance of achieving efficient green GaN-based LEDs without the use of wavelength converters has become higher in recent years, driven by increasing demand in a broad range of applications such as micro-LED displays [1, 2], high frequency visible light communication [3], compact lensless microscopes [4], high resolution optogenetic applications [5] etc. Therefore, an enhancement of the performance of green LEDs is of interest to both the industrial and research communities.

High-brightness green LEDs usually contain InGaN quantum wells (QWs) with high indium content, dependent on QW thickness. For 2 nm QWs, an indium content higher than 18% [6] is required. High indium fractions can be achieved by decreasing the InGaN growth temperature or by increasing the relative flux of the Indium precursor or a combination of both.

To understand the impact of InGaN growth temperatures on the optical properties, Hammersley *et al* [7] studied three blue and three green multiple QW (MQW) samples grown at different QW growth temperatures by photoluminescence (PL). For each set of samples, a reduction in the growth temperature was compensated by a decrease in the In-precursor flow in order to keep the InGaN composition as well as the PL peak emission constant. The QW growth temperature, the indium precursor flow rate, the average sample indium content (across the full well-barrier repeat), the peak emission energies and the internal quantum efficiency (IQE) values at 400 W cm^{-2} excitation power are shown in table 1. They observed lower

* To whom correspondence may be addressed.

Original content from this work may be used under the terms of the Creative Commons Attribution 4.0 licence. Any further distribution of this work must maintain attribution to the author(s) and the title of the work, journal citation and DOI.

 © 2021 The Author(s). Published by IOP Publishing Ltd Printed in the UK

Table 1. Sample series examined by Hammersley *et al* [7]. The same samples are studied in this paper.

Sample	QW growth temperature (°C)	TMI flow (sccm)	In content (%)	Peak emission energy (eV)	IQE (arb. u.)
Green 1	716	120	5.1 ± 0.5	2.40	0.33
Green 2	706	60	5.2 ± 0.5	2.37	0.28
Green 3	698	43	5.1 ± 0.5	2.36	0.22

IQE values with reduced QW growth temperatures for these samples. PL decay transients measured at low temperature indicated that the radiative lifetime within each set of samples was almost unaffected by growth temperature, but transients measured at 300 K showed faster decay rates for samples grown at lower QW growth temperatures. Hammersley *et al* ascribed the faster decays observed at 300 K to an increased rate of non-radiative recombination.

In this work, we have studied the microstructures of green MQW samples grown by the same conditions as those studied by Hammersley *et al* using scanning transmission electron microscopy (STEM) and cathodoluminescence (CL) techniques. A non-uniform CL emission intensity is observed on the sample surface, showing micron-size regions with weak emission intensities, the density of which is affected by the QW growth temperature. Similar emission property has been seen in CL and electroluminescence characterisations on LED devices by Wallace *et al* [8]. Submicron-scale spatial inhomogeneities of the optical properties of high indium content LEDs were also observed in confocal micro-PL images by Okamoto *et al* [9]. Such emission inhomogeneity implies local variations in the IQE of the MQW samples, which would influence the performance of related LED devices.

The STEM characterisation in this work demonstrates that regions with weaker emission intensities are associated with a smaller local density of gross well width fluctuations (GWWFs). For both blue [10] and green [11] LEDs, GWWFs have been suggested to improve the device performance. This article evaluates the connection among the QW growth temperatures, the distribution of GWWFs, and the IQE of green InGaN QWs, which provides an important insight into methods for improving green LED performance.

2. Experimental methods

We refer the reader to [7] for sample details, but note some specific points here: The conditions used for the QW growth in this article are common for the growth of the active region of green LED devices [11–13]. Though the InGaN QWs were grown at temperatures stated in table 1, quantum barriers were grown at a higher temperature. The advantages of this two-temperature growth method are discussed in [10]. The sample structure ends with the last GaN barrier, leaving the last QW about 10 nm below the sample surface.

Atomic force microscopy (AFM) analysis was carried out using a Veeco Dimension 3100 in tapping mode. The optical properties were studied by a FEI XL30 field-emission gun—scanning electron microscope (SEM), operated with a beam energy of 3 keV, connected to a Gatan MonoCL CL system. An FEI Tecnai Osiris was used for STEM structural analysis at 200 kV. The beam current and the exposure time used were 100 pA and 3 μs. The STEM specimen was prepared using a FEI Helios NanoLabTM focussed ion beam (FIB) by an *in situ* lift-out method using Ga ions accelerated at 30 kV followed by 5 kV surface treatment. The specimen was flat with a thickness of about 100 nm. There was no observable electron-beam damage throughout the experiment.

A multi-microscopy sample preparation method [14] was required for this study because the STEM specimen needs to be made at an appropriate location with a boundary between a bright and a dark patch in specimen position which can be identified in the STEM to allow any structural differences to be correlated with the CL data. The necessary experimental steps are as follows:

(a) Deposit a gold pattern to mark reference positions on the sample using a standard optical lithography process.
(b) Locate a dark patch in CL near a specific gold patch and identify the position of the boundary of the dark patch in the relevant secondary electron (SE) image in relation to the gold patch.
(c) Perform a line-scan measurement (see figure 5) centred at the CL dark patch boundary.
(d) Take an AFM scan at approximately the same area. The AFM data contains more accurate topographical information than the SE images and will be used to correlate surface features with features found in STEM images later. AFM images also allow us to identify the direction of atomic terraces. According to Jouvet *et al* [15], troughs in the QWs tend to align along the same direction as the surface terrace edges, which for our sample means parallel to [11–20]. TEM lamella should then be made such that their FIB-prepared surfaces are perpendicular to this direction. Imaging in the [11–20] zone axis then allows study of the gross-well width fluctuations in STEM without problems from projection effects.
(e) Locate the region previously line-scanned by the SE in the FIB and prepare a STEM lamella using the method described in [14]. The dark patch boundary is marked by a thicker protective Pt deposition.
(f) Make STEM observations on dislocations and compare with the AFM surface profile to check the exact specimen location on the sample.

3. Results and discussion

To examine the morphology of the QW samples, three 5×5 μm AFM scans are taken on every sample. Figure 1

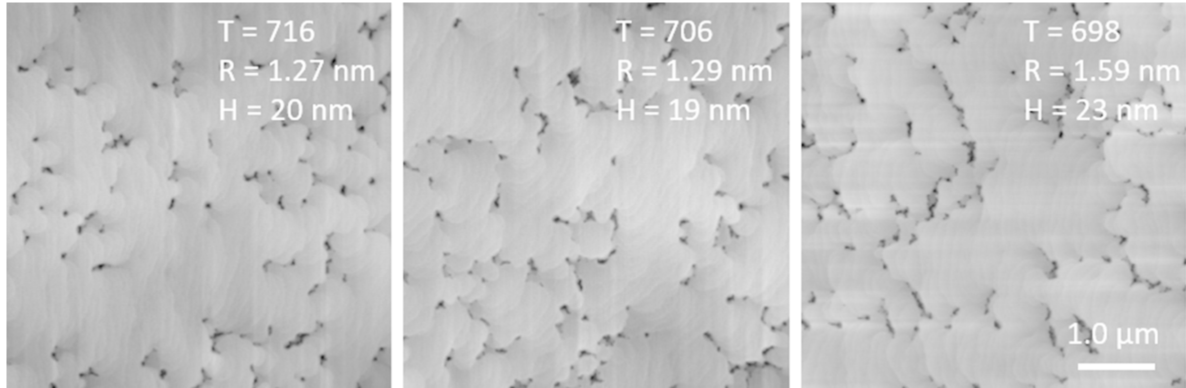

Figure 1. Shows the 5 × 5 μm AFM scans of the MQW samples revealing the surface morphology. The QW growth temperature (*T*), RMS roughness (*R*) and image height (*H*) are stated on the image. Note: *H* is the difference in height between the highest and lowest pixels in the image.

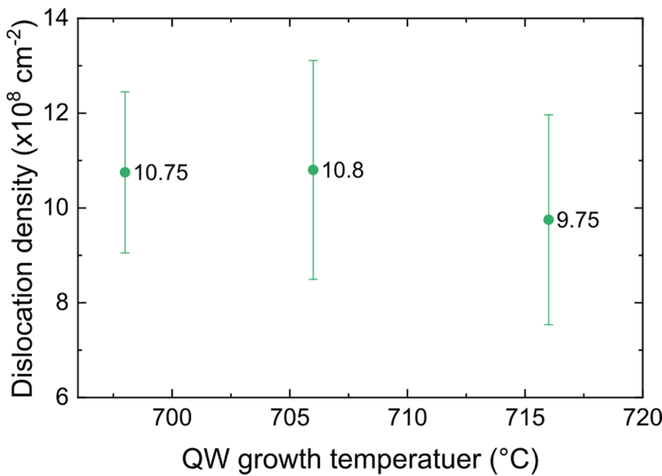

Figure 2. The density of dislocations against QW growth temperatures for the MQW samples.

shows the examples of them. All sample surfaces are smooth with root mean squared (RMS) roughness below 2 nm. Atomic bilayer steps can be seen across much of the surface of every sample and black spots are seen related to surface pits caused by the termination of threading dislocations (TDs). Such surface pits, known as V-pits or V-defects are commonly found in InGaN MQWs [16, 17]. In the growth of LEDs, these pits are often filled in during the deposition of the p-cap, resulting in devices with reasonable performance [18, 19]. V-pits often have {10-11} facet as sidewalls, and QWs formed on these sidewalls typically have smaller thickness and indium concentration than the surrounding *c*-plane QWs [16, 17]. Such {10-11} QWs can therefore act as energy barriers suppressing the lateral transportation of the carriers to dislocation cores. This self-screening behaviour at V-pits is one of the mechanisms which has been suggested to make nitride LEDs tolerant of a high density of TDs.

To further quantify the effect of TDs, the density of TDs of the MQW samples is estimated using an automatic program, PITS [20], on the nine AFM images. PITS normalises the images, calculates the derivatives in the image contrast and creates normalised derivative bitmaps, allowing TD pits to be identified by applying a threshold to the resulting image. However, as dislocation pits form clusters in our samples, PITS is used to identify dislocation clusters instead of individual dislocations. 1 × 1 μm AFM scans are taken for different dislocation clusters and the average number of TDs within a cluster is counted manually. The TD density of each sample is then calculated from the product of the number of clusters and the average number of TDs within a cluster, meaning that both factors contribute to the large errors on the TD density. The resulting data on the density of the TDs is summarized in figure 2.

The MQW samples have more than twice the TD densities of the pseudo-substrates. This difference in TD density may potentially be attributed to misfit dislocations (MDs) generated as a consequence of strain relaxation in the QWs [21]. MDs can be associated with (a + c)-type dislocations [22], which are additional TDs (2TDs per MD) in the QWs, and eventually lead to additional TD pits in the sample surface. A correlation between the dislocation density and the QW growth temperature cannot be observed from figure 2. TD density alone is therefore unlikely to be responsible for the observed change in the non-radiative recombination rates with QW growth temperature [7].

In order to study the emission characteristics and defects at a microscopic scale, SEM-CL is used to examine the sample surfaces. Examples of the CL images of the MQW samples are shown in figure 3.

The CL images of the samples become increasingly patchy as the QW growth temperature drops. Micrometer-sized dark patches were observed in all samples but particularly well-defined in the CL images of the sample with the lowest QW growth temperature (698 °C). Overall, the size of the dark patches, and the difference between the brightness of the light and dark regions increases as growth temperature decreases. Figure 4(a) highlights the CL emission of the sample with the lowest QW growth temperature from a typical dark patch (outlined in yellow) and also indicates examples of dark spots related to dislocations outside of the dark patch (circled in red).

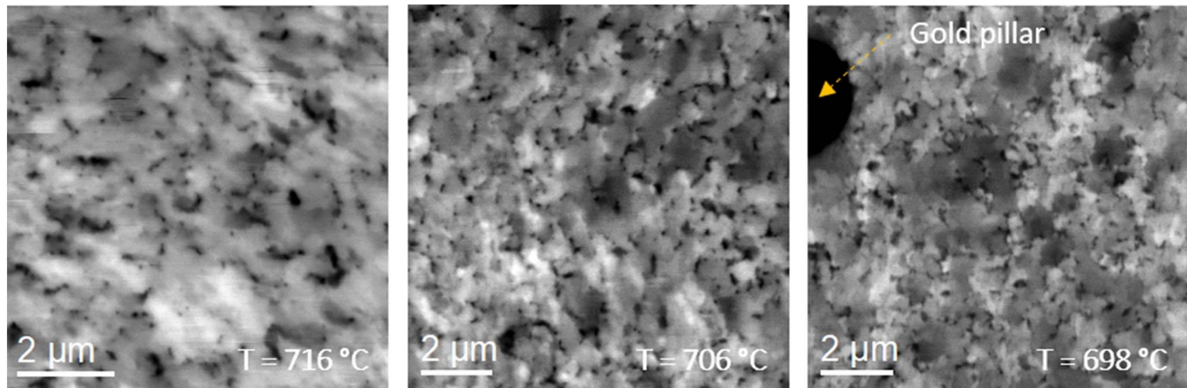

Figure 3. CL images of the MQW samples taken from the surface. The QW growth temperature (T) is stated on the image.

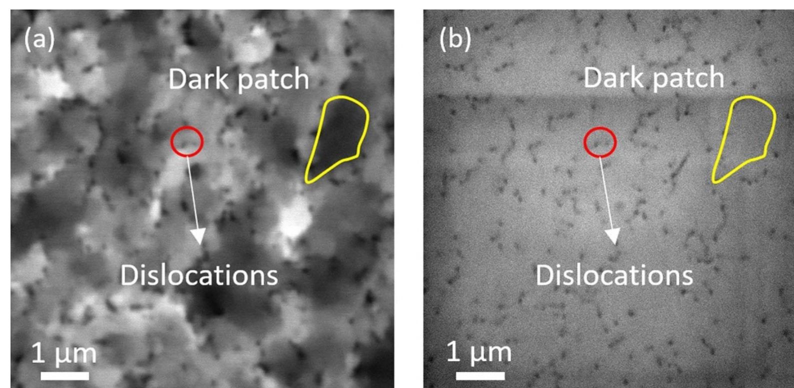

Figure 4. (a) CL image taken on the sample grown at 698 °C and (b) SE image taken on the same position of (a). Example dislocations are enclosed in the red circles and an example dark patch is highlighted by the yellow curve.

Figure 4(b) is the corresponding SE image taken at the same position. It should be noted that a large portion of the dark patch cannot be associated with any (cluster of) TDs seen in the SE image.

Spectral information comparing the dark patches and the bright areas can be obtained by recording CL spectra at multiple points along a line (a 'line scan'), across a dark patch boundary. Gaussian fits are applied over emission wavelengths from 490 to 590 nm and are fitted using the in-build function 'Gaussian Fit' function in Digital Micrograph. Peak emission amplitude and peak emission wavelength can be extracted from the Gaussian fits. Figures 5(a) and (b) are the peak emission amplitude profile and the peak emission wavelength profile of a typical CL line scan across the dark patch boundary. Two fitting examples taken from the dark patch and the bright area, respectively, are shown in figures 5(c) and (d). Though the position of the line scan is chosen to be having as few TDs as possible, the strain fields of two nearby TDs in the dark patch still affect the emission wavelength locally. The average emission amplitudes and wavelengths of the bright area and the dark patch, disregarding the regions near TDs, are highlighted by red dotted lines. The peak emission amplitude of the dark patch is, as expected, lower than that of the bright area. Additionally, the peak emission wavelength is red shifted by about 5 nm in the dark patches.

From figure 4(a), dark spots related to TDs can be clearly seen, with sizes from tens to a few hundred nanometres, consistent with the sub-micron minority carrier diffusion length which has been reported for GaN-based materials [23, 24]. The dark patches of a few micron extent therefore indicate emission properties that cannot result solely from the impact of TDs. Other factors, such as local variation in QW thickness and alloy composition, might be responsible for such non-uniform emission intensities. Multi-microscopy experiments are used to study the QW structure corresponding to the dark patches and compare it with the bright areas, as described in section 2.

The green 3 sample (with the lowest QW growth temperature) is the main subject of this part of the study as the dark patches are well defined in CL. One example of the multi-microscopy experiments is shown in figure 6, where figure 6(a) is the CL image including the line-scan, figure 6(b) is the AFM profile corresponding to the surface of the line-scan and figure 6(c) is the STEM high angle annular dark field (HAADF) image of the specimen made from the line-scan position. The dark line above the MQW layer in figure 6(c) indicates the surface of the sample and the material above the dark line is the Pt protective layer deposited in the FIB. The distances between dislocations found in the STEM HAADF image are consistent with those in the AFM line profile, as

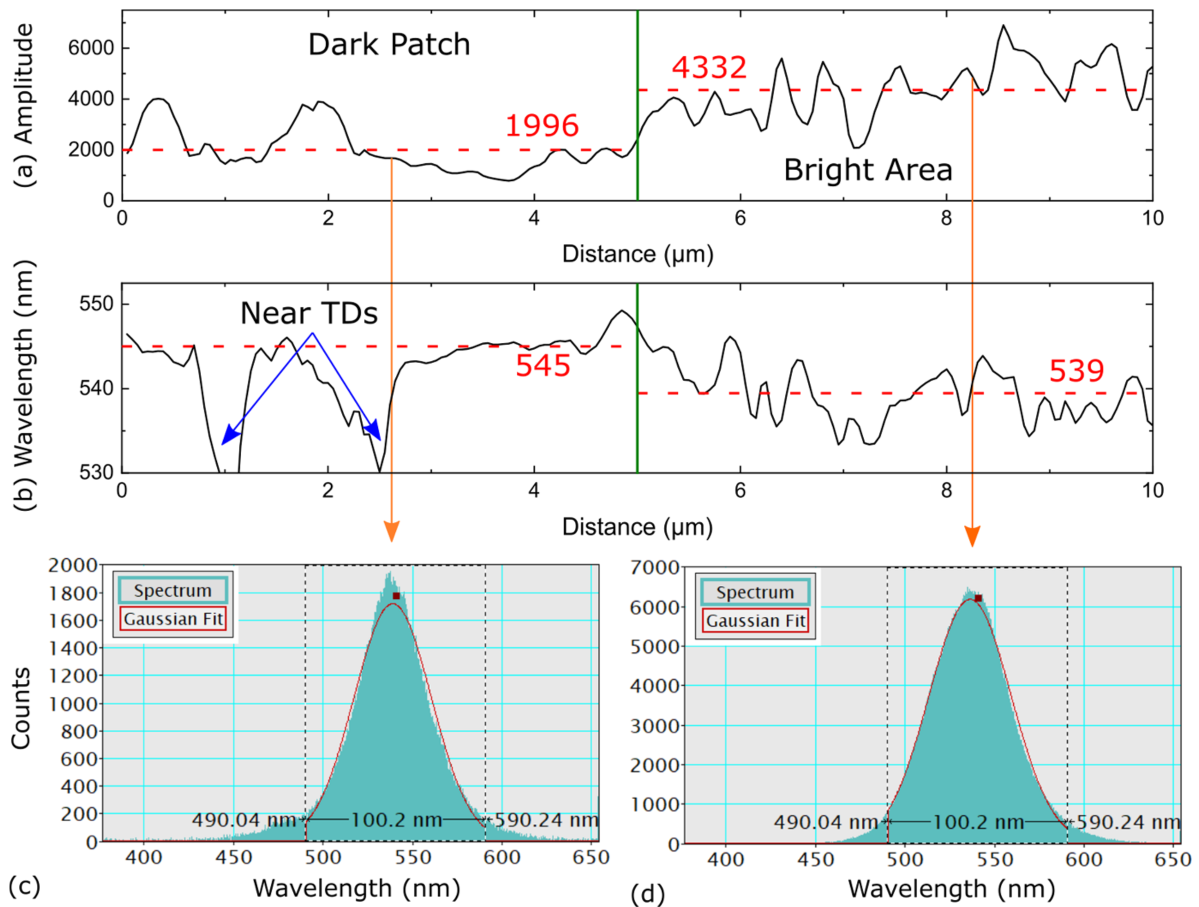

Figure 5. (a) The peak emission amplitude and (b) the peak emission wavelength obtained from a CL line scan performed on the sample grown at 698 °C across a dark patch boundary. Two fitting examples of the dark patch and the bright area are show in (c) and (d), respectively. The dark patch boundary is marked by the green lines. There are two large blue-shift peaks within the dark patch which are related with nearby dislocations. Disregarding the regions near TDs, the average emission amplitudes and wavelengths of the dark patch and the bright area are indicated by red dotted lines.

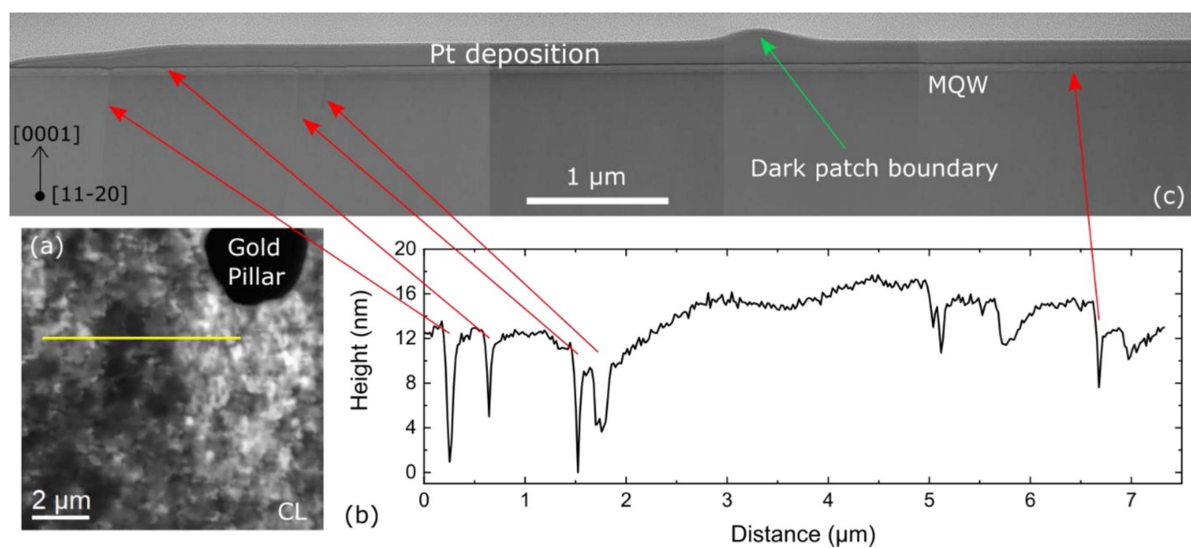

Figure 6. (a) The CL image taken in step 2. The line-scan position is highlighted by the yellow line. (b) The AFM profile corresponding to the line-scan position extracted from the AFM image taken in step 4. (c) The overview STEM HAADF image taken in step 6. Dislocations in (c) are matching with the dislocation pits found in (b). The dark patch boundary found in step 3 is marked by thicker Pt deposition on the sample surface, which is highlighted by the green arrow.

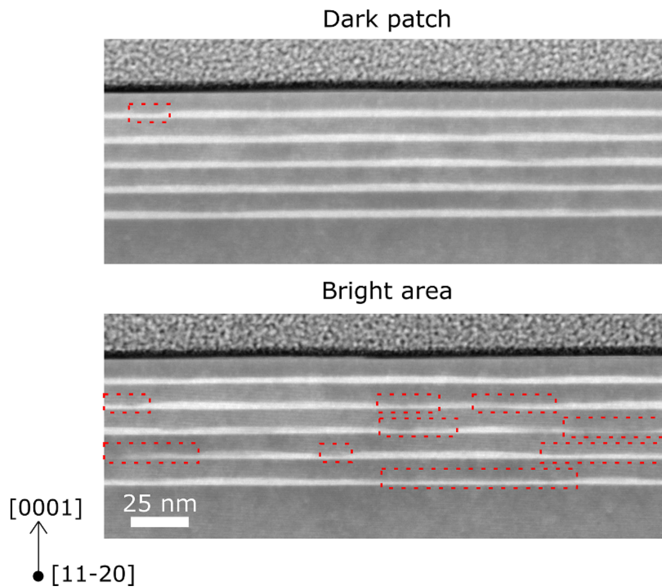

Figure 7. STEM HAADF images showing the MQW structure of the dark patch and the bright area in the sample grown at 698 °C. The bright lines show the positions of QWs. GWWFs are marked in red doted boxes. The material above the dark line is the Pt protective layer.

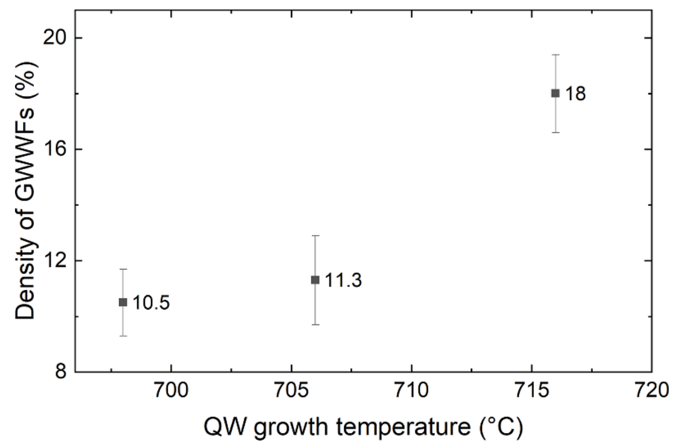

Figure 8. The average densities of GWWFs plotted against the QW growth temperatures.

indicated by the red arrows, illustrating that the specimen is prepared at the desired location.

HAADF STEM images of the MQW structures from the dark patch and adjacent bright area, taken in the [11–20] zone, are shown in figure 7. The QW structures are more intact in the dark patch but less uniform in the bright area. If we define a part of the QW where the width is less than half of the maximum width as a GWWF, the density of GWWFs can be calculated as the total length of all GWWFs (L_{GWWF}) divided by the length of QW measured (L_{QW}), L_{GWWF}/L_{QW}. Four images are taken on both the dark patch and the bright area, and the multi-microscopy experiment is repeated twice on different dark patches of green 3. The density of GWWFs in the bright area is 15.5% ± 1.5% and the density of GWWFs in the dark patch is 5.4% ± 1.4%. The bright areas consistently have larger density of GWWFs compared to the dark patch. STEM HAADF images were also taken from the cross-sections of green 1 and green 2 to estimate their average densities of GWWFs. However, as the dark patches are more difficult to define on these two samples, multi-microscopy measurements were not applied to them. The average densities of GWWFs of all three MQW samples are estimated in figure 8, which shows a reduction in the GWWF density as the QW growth temperature decreases.

The impact of GWWFs can be explained based on previous experimental results by Oliver *et al* [10]. They reported that the formation of GWWFs is due to exposure of unprotected InGaN to high temperatures during growth, which results in indium desorption. If GWWFs are regions with low indium content and thinner QW, they are a locally high bandgap area due to both the composition and the quantum confinement effect. In an early study of van der Laak *et al*, it was found that ~90% of the TDs pass through these high bandgap regions [11]. The activation energy of defect-related non-radiative recombination process was found to be about 55 meV for samples without GWWFs but 220 meV for samples with GWWFs [10]. Oliver *et al* therefore proposed that GWWFs in the QWs provide an additional barrier to carrier diffusion to defects.

The results from CL line scan (figure 5) support this theory. The brighter areas also emit at a shorter average wavelength, consistent with lower indium content and smaller thickness in the GWWF-containing areas. Less barriers to carrier diffusion to defect sites are very likely responsible for the weaker emission of the dark patches in sample green 3, where few or no GWWFs were observed.

TDs are however not likely to be the relevant defect sites for non-radiative recombination in the dark patches, since dislocation-related dark spots can be found in both the bright and dark regions and appear with similar density in each case. Instead, point defects could provide sites for non-radiative recombination [7] and GWWFs may impede carrier diffusion to these sites in much the same way they prevent carrier diffusion to dislocations [11]. Another possibility is that the process of desorption of indium rich InGaN could lead to preferential removal of point defects, leading to lower defect densities in the GWWF-containing regions, as indium rich regions have been reported to have a high point defect density [25].

It is also worth mentioning that blue-emitting QW samples have also been investigated by Hammersley *et al* [7], where higher QW growth temperatures were reported to lead to higher IQE values as well. However, our experiments indicate that dark patches are not found in these blue QW samples. Though emission inhomogeneities have been found in blue LEDs by others, both Wallace *et al* [8] and Okamoto *et al* [9] correlated lower emission intensities to higher emission energies, which is opposite to what we observed for green-emitting QW samples. Okamoto *et al* suggested that for low indium content LEDs, carrier localisation effects from indium-rich areas control the radiative recombination efficiency. Overall, this suggests that other mechanisms exist for the blue samples and the significance of these mechanisms in blue and green samples are different.

Although the underlying reasons for an inhomogeneous distribution of GWWFs in different regions of the same green QW sample are still unclear, the fact that samples grown at low temperatures show fewer GWWFs is potentially due to a smaller thermal budget available to drive the indium desorption. Other than increasing the QW growth temperature, a temperature ramp between the growth of QW and quantum barrier could provide a similar thermal budget for the removal of some QW material to form GWWFs [10]. Introducing H_2 to the carrier gas during growth of the GaN barrier has also been shown to cause discontinuous QWs that are narrower and of lower indium content [26]. Additionally, as GWWFs are mostly aligned with the surface terrace edges [15], which are related to the substrate miscut, the formation of GWWFs can be affected by substrate miscut angles. Massabuau *et al* [27] demonstrated that a change of the substrate miscut angle from 0° to 0.5° increases the density of GWWFs. These methods of engineering GWWFs in the LED structure are also promising in achieving more efficient *c*-plane green LEDs.

4. Conclusions

The SEM-CL measurements show large dark patches that do not correspond to TDs. As the QW growth temperature decreases, the contrast between the light and dark patches increases and the dark patches become larger. STEM structural analysis of dark patches occurring in sample green 3 indicate that they have fewer GWWFs compared to the bright regions. A higher density of GWWFs is found in the samples grown at a higher QW growth temperature with higher IQEs. Since the distribution and density of GWWFs plays an important role in the effect of QW growth temperature to the IQE of green LEDs, increasing GWWFs density by altering various growth conditions, such as QW growth temperature, temperature ramp, carrier gas composition and substrate miscut angle, presents a useful option to improve the performance of green LEDs.

Acknowledgments

We would like to acknowledge funding from the Engineering and Physical Sciences Research Council (EPSRC) under EP/M010589/1. The data that support the findings of this study are openly available in the University of Cambridge repository at https://doi.org/10.17863/CAM.56641.

ORCID iD

B Ding https://orcid.org/0000-0003-2868-3416

References

[1] Wasisto H S, Prades J D, Gulink J and Waag A 2019 *Appl. Phys. Rev.* **6** 041315
[2] Templier F 2016 *J. Soc. Inf. Display* **24** 669
[3] Rajbhandari S, McKendry J J D, Herrnsdorf J, Chun H, Faulkner G, Haas H, Watson I M, O'Brien D and Dawson M D 2017 *Semicond. Sci. Technol.* **32** 023001
[4] Heer R, Krieger S, Geleff S, Schotter J, Wu W, Scholz G and Wasisto H S 2018 *Proceedings* **2** 1074
[5] Poher V *et al* 2008 *J. Phys. D: Appl. Phys.* **41** 094014
[6] Damilano B and Gil B 2015 *J. Phys. D: Appl. Phys.* **48** 403001
[7] Hammersley S, Kappers M J, Massabuau F C P, Sahonta S-L and Dawson P 2015 *Appl. Phys. Lett.* **107** 132106
[8] Wallace M J, Edwards P R, Kappers M J, Hopkins M A, Oehler F, Sivaraya S, Allsopp D W E, Oliver R A, Humphreys C J and Martin R W 2014 *J. Appl. Phys.* **116** 033105
[9] Okamoto K, Kaneta A, Kawakami Y, Fujita S, Choi J, Terazima M and Mukai T 2005 *J. Appl. Phys.* **98** 064503
[10] Oliver R A *et al* 2013 *Appl. Phys. Lett.* **103** 141114
[11] van der Laak N K, Oliver R A, Kappers M J and Humphreys C J 2007 *Appl. Phys. Lett.* **90** 121911
[12] Chang S J, Lai W C, Su Y K, Chen J F, Liu C H and Liaw U H 2002 *IEEE J. Sel. Top. Quantum Electron.* **8** 278
[13] Huang C-F, Liu T-C, Lu Y-C, Shiao W-Y, Chen Y-S, Wang J-K, Lu C-F and Yang C C 2008 *J. Appl. Phys.* **104** 123106
[14] O'Hanlon T J, Bao A, Massabuau F C-P, Kappers M J and Oliver R A 2020 *Ultramicroscopy* **212** 112970
[15] Jouvet N, Kappers M J, Humphreys C J and Oliver R A 2013 *J. Appl. Phys.* **113** 063503
[16] Hangleiter A, Hitzel F, Netzel C, Fuhrmann D, Rossow U, Ade G and Hinze P 2005 *Phys. Rev. Lett.* **95** 127402
[17] Tomiya S, Kanitani Y, Tanaka S, Ohkubo T and Hono K 2011 *Appl. Phys. Lett.* **98** 181904
[18] Liu M, Zhao J, Zhou S, Gao Y, Hu J, Liu X and Ding X 2018 *Nanomaterials* **8** 450
[19] Xu C, Zheng C, Wu X, Pan S, Jiang X, Liu J and Jiang F 2019 *J. Semicond.* **40** 052801
[20] Bennett S E, Holec D, Kappers M J, Humphreys C J and Oliver R A 2010 Imaging dislocations in gallium nitride across broad areas using atomic force microscopy *Rev. Sci. Instrum.* **81** 063701
[21] Graham D M, Dawson P, Godfrey M J, Kappers M J, Costa P M F J, Vickers M E, Datta R, Humphreys C J and Thrush E J 2006 *Phys. Status Solidi* c **3** 1970
[22] Liu R, Mei J, Srinivasan S, Omiya H, Ponce F A, Cherns D, Narukawa Y and Mukai T 2006 *Japan. J. Appl. Phys.* **45** L549
[23] Bandić Z Z, Bridger P M, Piquette E C and McGill T C 1998 *Appl. Phys. Lett.* **72** 3166
[24] Yakimov E 2015 *J. Alloys Compd.* **627** 344
[25] Uedono A, Ishibashi S, Oshima N, Suzuki R and Sumiya M 2014 *ECS Trans.* **61** 19
[26] Ren X, Riley J R, Koleske D D and Lauhon L J 2015 *Appl. Phys. Lett.* **107** 022107
[27] Massabuau F C-P, Tartan C C, Traynier R, Blenkhorn W E, Kappers M J, Dawson P, Humphreys C J and Oliver R A 2014 *J. Cryst. Growth* **386** 88